Corrosion Science 158 (2019) 108102

Contents lists available at ScienceDirect

Corrosion Science

journal homepage: www.elsevier.com/locate/corsci

Enhanced interfacial bonding and superior oxidation resistance of CoCrAlY-TiB_2 composite coating fabricated by air plasma spraying

Qi An[b], Lujun Huang[a,b,*], Shaolou Wei[b,1], Rui Zhang[b], Xudong Rong[b], You Wang[b], Lin Geng[a,b,*]

[a] State Key Laboratory of Advanced Welding and Joining, Harbin Institute of Technology, P.O. Box 433, Harbin, 150001, PR China
[b] School of Materials Science and Engineering, Harbin Institute of Technology, Harbin, 150001, PR China

ARTICLE INFO

Keywords:
Air plasma spray
CoCrAlY-TiB_2 composite coating
Microstructures
Bonding strength
Cyclic oxidation

ABSTRACT

In order to enhance oxidation resistance of titanium matrix materials, CoCrAlY-TiB_2 coating is introduced by air plasma spray. Tensile test demonstrates that TiB_2 addition promoted interfacial bonding strength with a maximum enhancing effect of 22.6%, which alleviated mechanical spallation of the coating and consequently gave rise to the improved physicochemical stability. Cyclic oxidation tests at 700, 800, and 900 °C reveal that weight gain of coated specimens reduced by 66.7%, 73.1%, and 75.2% compared with the TMCs substrate. The significantly enhanced anti-oxidation performance was mostly ascribed to the improved microstructural stability and the formation of dense Al_2O_3 and Cr_2O_3 oxides.

1. Introduction

Based on the superior properties, such as high specific strength and stiffness together with outstanding chemical corrosion resistance, titanium matrix composites (TMCs) are considered as promising candidates for structural components in automobile, aviation, and aerospace engineering. However, the discontinuously reinforced titanium matrix composites (DRTMCs) with a homogeneous reinforcer distribution often inevitably suffered from ambient temperature embrittlement challenge, limiting the scope of potential application in multiple fields [1–3]. To combat this problem, it has been documented in literature that the DRTMCs with a special quasi-continuous network architecture fabricated through a cost-effective powder metallurgy (PM) method exhibited appreciable ductility and excellent strength, which overcame the bottleneck problem of DRTMCs, leading to better strength-ductility synergy [2,4,5]. Unfortunately, even though the chemically stable ceramic reinforcements were beneficial for the improvement of oxidation resistance [6], the presence of large volume fraction of titanium matrix still exhibited strong propensity for oxidization especially in the atmosphere environment beyond 550 °C [7,8]. With regard to this, further enhancing the oxidation resistance of network-strengthened TMCs and thereby promoting their service temperature will require the introduction of suitable anti-oxidation coatings.

Coating material systems like aluminide [9], Ti-Al-X (X = Cr, Nb, N) [10], silicide ceramics [11], and MCrAlY (M = Ni, Co, or NiCo) [12–14] were previously reported to possess better oxidation resistance. The most promising candidate amongst them is the MCrAlY alloy showing desirable ductility, high strength, outstanding anti-oxidation performance, and hot corrosion resistance at elevated temperatures [15]. In particular, the slowly formed dense Al_2O_3 film and the coating microstructures suppressed elemental diffusion, contributing to excellent oxidation resistance [16]. MCrAlY also has capability to produce a continuous and adherent thermally grown oxide (TGO), as well as good cracking/spallation resistance. As a result, this sort of coating system demonstrated the potential to be employed as bond coatings in thermal barrier coating (TBC) application. The commonly used processing methods for MCrAlY coating include: air plasma spray (APS) [12,17,18], vacuum plasma spray (VPS) [19], high velocity oxygen fuel deposition (HVOF) [20], magnetron sputtering [21], electron beam physical vapor deposition [16], and laser deposition [22,23]. Among them, the air plasma spray technique is considered as a suitable method to produce the coatings, because of its appreciable tunability and desirable cost-effectiveness [24]. For instance, Vermaak et al. produced the γ' strengthened MCrAlY coating by plasma spraying, which presented superior adherence than the NiAl-based coatings [15]. Chen et al. studied the effect of alloying elements (Ta, Mo) on the microstructures and properties of NiCoCrAlY coating by APS technology, revealing that Ta addition improved the oxidation resistance, and Mo addition enhanced the adhesion between coating and substrate [12,17]. Furthermore, it was reported that post treatments could also modify the

* Corresponding authors at: State Key Laboratory of Advanced Welding and Joining, Harbin Institute of Technology, P.O. Box 433, Harbin, 150001, PR China.
E-mail addresses: huanglujun@hit.edu.cn (L. Huang), genglin@hit.edu.cn (L. Geng).
[1] Present address: Department of Materials Science and Engineering, Massachusetts Institute of Technology, Cambridge, MA 02139, USA.

https://doi.org/10.1016/j.corsci.2019.108102
Received 28 February 2019; Received in revised form 10 July 2019; Accepted 14 July 2019
Available online 19 July 2019
0010-938X/

MCrAlY coating. For example, Cai et al. found that the high-current pulsed electron beam irradiation refined the grains of as-sprayed CoCrAlY coating, effectively improving the oxidation resistance [25]. Deng et al. reported that the cathode plasma electrolysis treatment also enhanced the anti-oxidation performance of thermal sprayed NiCoCrAlY bond coat [18].

In this work, the anti-oxidation CoCrAlY coating was designed and fabricated on the network structured 3.4 vol.% TiBw/Ti64 composites with the purpose of enhancing the maximum service temperature of TMCs over 800 °C. Our main focus is to examine the coatings' endurability to more aggressive environment. In order to modulate the coating microstructures and the interfacial bonding strength between the coating and substrate, a small number of TiB_2 powder was introduced to the CoCrAlY coating system by low-energy ball milling and APS techniques. Additionally, a novel surface roughing method (termed "surface etching pretreatment" in the following) was employed in this study before spraying to improve the bonding strength. Compared with the traditional surface grit blasting process, the surface etching pretreatment is characterized by its low energy consumption, high efficiency and good economic feasibility. Subsequently, the interfacial bonding strength between the coating and substrate has been studied through the uniaxial tensile test, and APS power input is optimized. Furthermore, the cyclic oxidation behavior of CoCrAlY-TiB_2 composite coating has been investigated, and the corresponding oxidation mechanisms are further elucidated.

2. Experimental

2.1. Materials and deposition

The substrate material used in this study was as-sintered 3.4 vol.% TiBw/Ti64 composites with a dimension of 10 cm × 10 cm × 2 cm. Commercially available CoCrAlY powders with D_{50} = 50 μm (Fig. 1(a)) and fine prismatic TiB_2 powders (D_{50} = 3 μm as shown in Fig. 1(b)) were selected as raw materials in this work. The nominal composition of the CoCrAlY powder is Co-24.83-Cr12.74Al-2.68Ta-1.34Si-1.06Y (wt.%). Then the CoCrAlY-1TiB_2 (wt.%) composite powders were mixed through ball milling at a speed of 200 rpm for 8 h. From Fig. 1(c), it can be seen that CoCrAlY powder with a diameter between 37–65 μm after ball milling exhibited the similar morphology and size of raw CoCrAlY powder, indicating negligible plastic deformation has taken place. Meanwhile, some tiny particles were adhered to the CoCrAlY powder surface. Table 1 summarizes the chemical analyses of CoCrAlY-TiB_2 powder (Fig. 1(c)), revealing that the elements of zones "2, 3" mainly consisted of Ti and B. Therefore, it is realized that fine TiB_2 powders were adhered onto the surface of CoCrAlY powder during ball milling. The corresponding schematic of the composite powder is shown in Fig. 1(d). Subsequently, the APS equipment was employed to produce the CoCrAlY coatings with a spray distance of 100 mm under various energy input. Before deposition, the substrate material was preheated by the plasma spraying gun to improve the surface activity and decrease the temperature difference between substrate and the spraying powders.

Table 1
Chemical composition of powder zones marked "1-4" in Fig. 1 (at. %).

Point	Co	Cr	Al	Ta	Y	Ti	B	Si
1	45.81	19.96	27.80	0.74	3.44	–	–	2.24
2	6.19	3.60	2.92	–	0.49	27.62	59.17	–
3	0.50	0.36	0.18	–	–	30.85	68.11	–
4	48.74	23.91	23.63	0.74	0.60	–	–	2.38

2.2. Microstructural characterization

The cross section of the coatings was polished by SiC sand paper of grades 120, 400, 800, 1200, 1500# and cleaned by ethanol. Then a Zeiss SUPRA 55 scanning electron microscope (SEM) equipped with energy dispersion X-ray spectroscopy (EDS) system was employed to characterize the morphology, microstructures, and elemental distribution of the as-sprayed coatings before and after cyclic oxidation tests. In addition, a D/Max-2400 X-ray diffractometer (XRD, Cu K_α) was utilized to identify phase constitutions of the coatings before and after the oxidation tests.

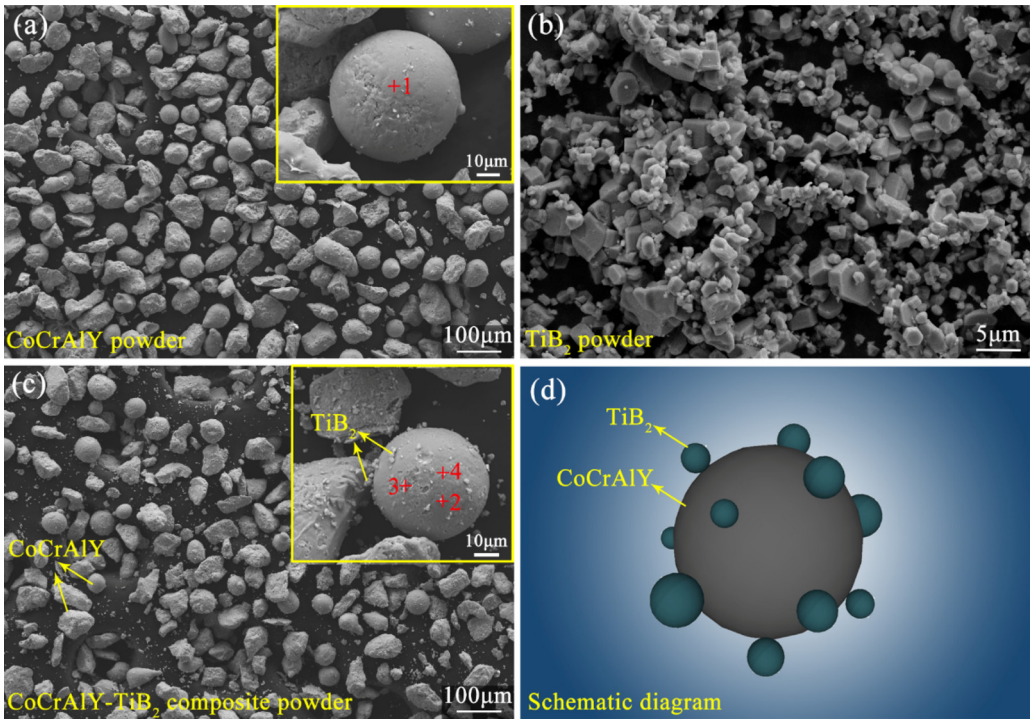

Fig. 1. SEM micrographs of (a) coarse CoCrAlY powders, (b) fine TiB_2 powders, (c) CoCrAlY-TiB_2 composite powders, and (d) schematic of the composite powder.

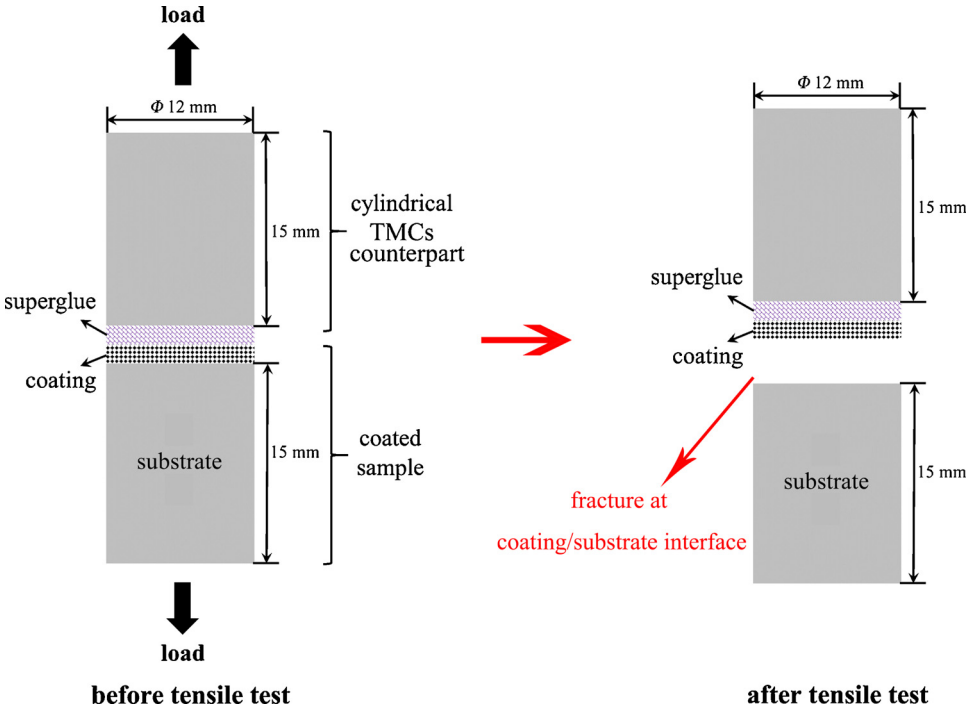

Fig. 2. Schematic of the samples before and after tensile test.

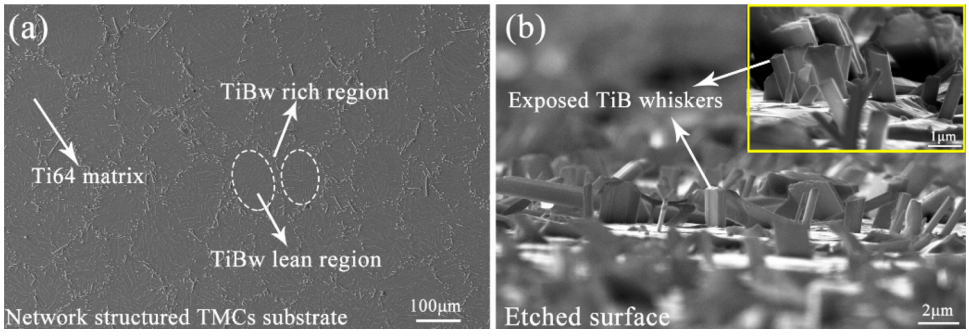

Fig. 3. Microstructures of the network structured TMCs substrate (a), and the etched surface (b).

2.3. Bonding strength test

According to the ASTMC633-79 test standard [26], the interfacial bonding strength (namely interfacial bonding strength between coating and substrate, for simplicity, it is described as "bonding strength" in the rest of the text) was analyzed with INSTRON-5569 universal material testing machine at a tensile loading rate of 0.5 mm·min^{-1}. Three specimens with each parameter were tested to ensure reproducibility. Fig. 2 illustrates the assembly diagram of the tensile test sample, revealing that the coated cylindrical specimen and a cylindrical TMCs counterpart were glued together by 3 M superglue with a strength of 60 MPa, which was sufficient to measure the bonding strength. After tensile test, the samples fractured at the coating/substrate interface. The bonding strength was then evaluated based on these tensile data.

2.4. Cycle-thermal oxidation test

The specimens for high-temperature oxidation experiments were prepared through the following method: two planes of the cubic-shaped TMCs substrate with the dimension of 10 cm × 10 cm were both coated by APS process. Later on, the cyclic oxidation tests were carried out in a muffle furnace at 700 °C, 800 °C and 900 °C with a heating rate of 20 °C·min^{-1} for a total duration of 100 h in air atmosphere respectively. The samples were placed inside alumina crucibles during the test, which were removed from the furnace at a regular interval and air-cooled to room temperature. In this work, the first two cycles were 5 h each, which were followed by the subsequent nine cycles of 10 h each. The weight was monitored using a PTX-FA210 high accuracy electronic balance with a precision of 0.1 mg after each cycle. Meanwhile, the phase constitutions were identified every 20 h. Additionally, the uncoated TMCs substrate was also tested for comparison. Three samples of each cycle were tested, and the average mass gain value is presented in this work.

3. Results and discussion

3.1. Surface pretreatment

It can be seen that TiB whiskers presented a network configuration (Fig. 3(a)) in the substrate material produced by powder metallurgy. The corresponding in situ chemical reaction mechanisms have been demonstrated elsewhere [4]. In order to improve the interfacial bonding strength, the substrate surface roughness was increased through etching pretreatment with a 5HF-15HNO_3 (vol.%) aqueous solution. Before spraying, the etched substrates were ultrasonically cleaned in ethanol bath. Fig. 3(b) shows the microstructures of

Table 2
The bonding strength between coating and substrate under different energy input.

Substrate	Samples	Energy (kW)	Coatings	Bonding strength (MPa)
3.4 vol.% TiBw/Ti64 composites	1#	24.75	CoCrAlY	18.76 ± 0.3
	2#	24.75	CoCrAlY-TiB_2	16.64 ± 0.5
	3#	27.50	CoCrAlY	22.61 ± 0.5
	4#	27.50	CoCrAlY-TiB_2	26.25 ± 0.6
	5#	30.25	CoCrAlY	25.13 ± 0.4
	6#	30.25	CoCrAlY-TiB_2	27.63 ± 0.4
	7#	33.00	CoCrAlY	22.52 ± 0.5
	8#	33.00	CoCrAlY-TiB_2	25.48 ± 0.7
	9#	35.75	CoCrAlY	15.63 ± 0.5
	10#	35.75	CoCrAlY-TiB_2	19.17 ± 0.3

substrate surface (TiBw/Ti64 composites) after surface etching pretreatment with an etching time of 20 s. It was evident that a large number of TiB whiskers was partially exposed on substrate surface after the elimination of Ti matrix, of which the average exposed length was around 2 μm (Fig. 3(b)). Besides, the exposed TiB whiskers exhibited slant angles on the surface, which was beneficial for pinning the coating and enhancing the bonding strength.

3.2. Optimization of the power input

The APS power input can directly influence the joining behavior and thereby properties of the spraying powders [27]. With this regard, the CoCrAlY and CoCrAlY-TiB_2 composite powders were deposited under various power input to optimize the bonding strength, and the selected parameters are listed in Table 2. The measeured interfacial bonding strength in Fig. 4 indicates the CoCrAlY-TiB_2 coating exhibited lower bonding strength than the coating without TiB_2 addition at 24.75 kW, which was due to the insufficient energy. Under such condition, the TiB_2 particles could not react with titanium and deteriorated the interfacial bonding strength. Subsequently, the CoCrAlY-TiB_2 composite coating presented comparatively higher bonding strength compared with that of the CoCrAlY when the energy was higher than 27.50 kW. During the spraying process with proper power input, the molten powders collided the substrate surface through a high-velocity inert gas flow. Moreover, the heated TiB_2 also contacted and reacted with Ti64 matrix of the substrate under a certain power input, forming localized metallurgical cohesion with the substrate. Consequently, the bonding strength was higher than that of the CoCrAlY coating without TiB_2 addition, and the maximum enhancing effect was about 22.6% at

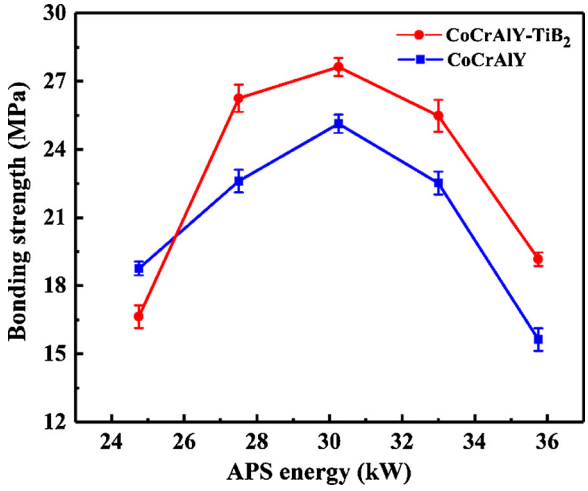

Fig. 4. The interfacial bonding strength of the coated samples under different power input.

35.75 kW.

Furthermore, Bonding strengths of both types of coatings exhibited improving trends and peak at 30.25 kW power input (25.13 (5#) and 27.63 (6#) MPa), exceeding which boding strengths subsequently decreased with respect to increasing power input. Fig. 5 shows the interfacial microstructures of the coatings deposited under various power inputs. The powders of 2# sample were not fully melted and the corresponded thickness was inhomogeneous. Solid-state sintering areas were also frequently formed at the interface during deposition (Fig. 5(a, b)) due to the insufficient power, which mainly consisted of heavy elements such as Co and Cr according to the EDS results (Table 3) and was detrimental to the bonding strength. Besides, Ti and B elements were also detected in some solid-state sintering areas (area "2″), and it was deduced as the existance of unmelted TiB_2 powders. In addition, the coating materials were fully melted generating a thickness of around 45–60 μm as the power input increased to 30.25 kW (Fig. 5(d)). The coating density was remarkably improved contributing to the bonding strength. However, the plasma jet under extensive energy input (35.75 kW) with enhanced falme flow rate interacted with the adjacent air forming a local vortex, which destroyed the stability of the plasma jet and sharply reduced the coating thickness to about 23 μm in Fig. 5(f). Consequently, a plasma power between 27.5–33 kW was optimized to improve bonding strength.

According to the XRD patterns presented in Fig. 6, the CoCrAlY-1TiB_2 (wt.%) composite coatings were composed of TaC, SiC Co_3Ti, $CrSi_2$, CrB_2, Al-rich β-(Co, Cr)Al and γ-(Co, Cr) solid solution (ss) phases. With the increase of power input, the intensity of diffraction peaks (2θ = 43.2°, and 50.5°) was greatly enhanced while the intensity of peak (2θ = 44.5°) was notably decreased, indicating that the content of Al-rich β-Al(Co, Cr) and γ-(Co, Cr) solid solution phases changed. Additionally, the temperature of the melted powders was also increased with enhanced energy input, which caused a relatively more sufficient diffusion. Since the coating mainly consisted of solid solution phases, various temperatures resulted in a small difference on the solid solubility for these phases. Moreover, higher temperature also led to relatively higher residual stress after rapid solidification. As a result, the XRD peaks also showed a little bit displacement at various power input. The Co_3Ti and CrB_2 phases were also gradually formed. Consequently, the desired phase constituents reported previously [20] could be prepared by the APS technology with appropriate flame temperature and dwell time.

The detailed microstructures of the as-sprayed CoCrAlY-TiB_2 composite coating with the optimized plasma power of 30.25 kW is shown in Fig. 7. It can be seen that most of the CoCrAlY-TiB_2 raw powders have been melted, and no obvious cracks and other imperfections were produced except for few tiny pores on the coating surface as a general characteristic of the APS technique (Fig. 7(a)). In addition, the surface SEM images were dealt and analyzed by ImageJ software, revealing the surface porosity of this coating was only 4.67%. Fig. 7(b) shows the dense microstructures with laminated feature were formed in the coating along depth direction which was characterized as the typical morphology by APS technique. Additionally, a relatively well bonded interface was generated (Fig. 7(c)). As shown in Fig. 7(d,e), a small number of liquid sintering and solid sintering areas also existed in the coating. The corresponding EDS line profile in Fig. 7(b) reveals that the dark phase in the laminated microstructure were mainly composed of Al and O, while the bright phases consisted of Co and Cr elements. In addition, the chemical composition of different regions marked as "1-6″ in Fig. 7 is also listed in Table 4, confirming that four typical phases (Al_2O_3, TaC, γ-(Co, Cr)ss and β-Al(Co, Cr)ss, respectively) were formed in the coating. During APS deposition process, the air can react with the surface of the melted liquid drop. Among all the elements in the coating, Al exhibits a strong thermodynamic tendency of oxidation, leading to the formation of Al_2O_3 as a dark phase of region "1″ (Fig. 7(b)). While two different solid solution phases were generated at the inner liquid drop as a result of rapid solidification, the gray phase of

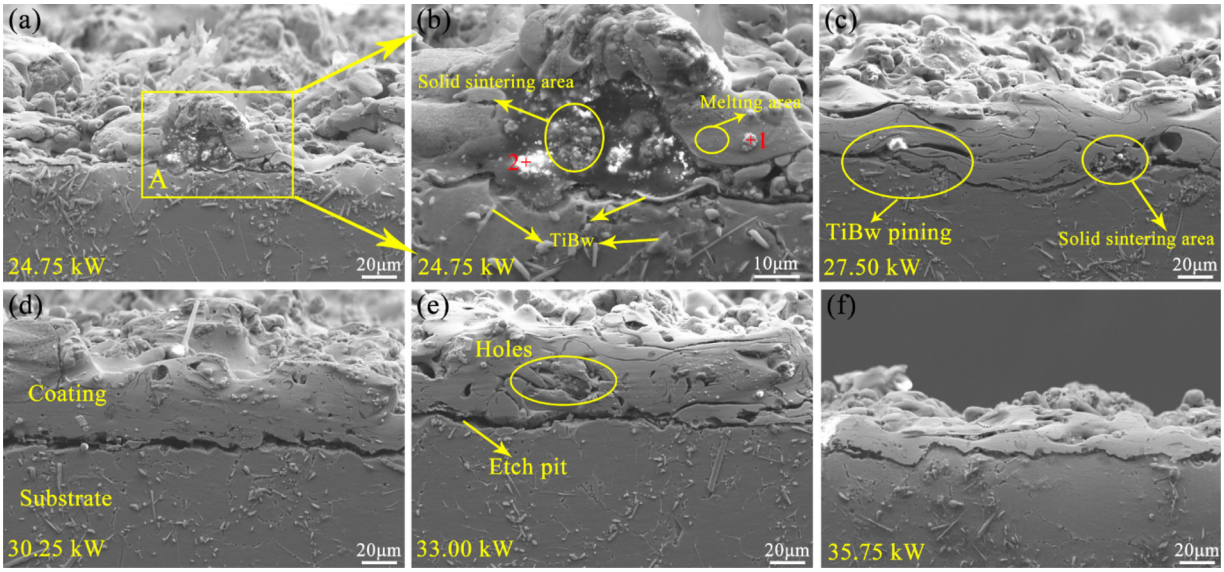

Fig. 5. The cross sectioned area of CoCrAlY-TiB_2 composite coating samples produced with different energy: (a) 2#; (b) higher magnification of zone "A" in Fig. 5(a); (c) 4#; (d) 6#; (e) 8#; (f) 10#.

Table 3
Chemical composition of points "1, 2″ in Fig. 5(b) (at. %).

Point	Co	Cr	Al	Ta	Y	Ti	B	Si	O	C
1	17.57	13.25	–	27.68	–	–	–	–	5.87	35.63
2	20.47	15.69	3.72	3.46	0.6	9.74	27.82	2.38	6.72	9.45

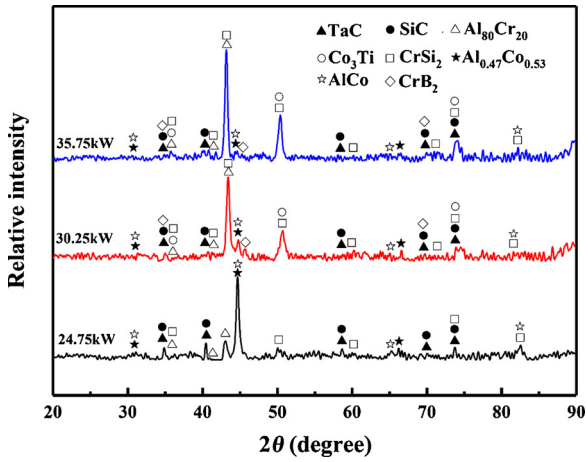

Fig. 6. The XRD patterns of the coatings fabricated under different plasma power.

region "2″ (Fig. 7(c)) was considered as the Al-rich β-Al(Co, Cr)ss, and the bright phase of region "3″ (Fig. 7(c)) was summarized as the γ-(Co, Cr)ss. Furthermore, a small quantity of white particles (region "4″ and "6″) considered as TaC phase were also generated in the coating, which was beneficial for enhancing the coating strength.

3.3. Cyclic oxidation experiment

The cyclic oxidation kinetics of uncoated TiBw/Ti64 substrate and TMCs coated with CoCrAlY-TiB_2 composite coating at various temperatures are demonstrated in Fig. 8. The substrate suffered from a rapid oxidation stage at the first 10 h. Then the weight gain value obviously decreased but still followed a linear oxidation law. As a result, the substrate material exhibited an unstable oxidation phenomenon throughout the test, and the mass gain per unit area after oxidation for 100 h at 700 °C, 800 °C, and 900 °C reached about 10.5 $mg{\cdot}cm^{-2}$, 14.9 $mg{\cdot}cm^{-2}$, and 24.5 $mg{\cdot}cm^{-2}$ (Fig. 8(a–c)). However, the TMCs coated with CoCrAlY-TiB_2 experienced a stable oxidation after the initial relatively rapid mass gain stage, following the parabolic rate rule upon the whole procedure. After the cyclic oxidation for 100 h, the corresponding weight gain of the coated specimens was only 2.5 $mg{\cdot}cm^{-2}$, 4.0 $mg{\cdot}cm^{-2}$, and 5.4 $mg{\cdot}cm^{-2}$. Compared with the uncoated substrate, the gained weight was remarkably reduced by 66.7%, 73.1%, and 75.2%.

Moreover, Fig. 8(a1–c1) also show the corresponding first derivative curves of the mass-gain value to quantitatively describe the mass-gain rate over oxidation time. These curves also proved that the TMCs substrate presented higher mass-gain rate compared with the coated specimen. For instance, the initial rate of substrate at 700 °C was about 0.4 $mg{\cdot}cm^{-2}h^{-1}$ (Fig. 8(a1)), which was two times faster than the coated one (around 0.2 $mg{\cdot}cm^{-2}h^{-1}$). Subsequently, the mass-gain rate decreased and the substrate exhibited a relatively constant rate of around 0.08 $mg{\cdot}cm^{-2}h^{-1}$ after 20 h, while the rate of CoCrAlY-TiB_2 coated sample was stable and close to only 0.01 $mg{\cdot}cm^{-2}h^{-1}$. Therefore, the mass-gain rate of the CoCrAlY-TiB_2 coated sample was obviously lower than the TiBw/Ti64 substrate, implying the oxidation resistance can be remarkably enhanced by introducing the CoCrAlY-TiB_2 coating. In addition, the mass-gain rate of the substrate at high temperatures also experienced a moderate increasing trend after the inflection points "A" (70 h at 800 °C in Fig. 8(b1)) and "B" (60 h at 900 °C in Fig. 8(c1)). When the TMCs substrate was cyclically oxidized at elevated temperature, the oxide scale spalled and detrimentally leading to the exposed fresh surface which was easily oxidized and then caused the inflection points of the mass-gain rate curve. Nevertheless, the rate of the CoCrAlY-TiB_2 coated sample exhibited a comparatively stable trend after the initial 20 h. Consequently, the CoCrAlY-TiB_2 coating presented stable and excellent anti-oxidation performance contributing to expanding the application fields of TMCs.

Subsequently, the XRD patterns of CoCrAlY-TiB_2 composite coating during the cyclic oxidation at different temperatures are shown in Fig. 9. A common phenomenon can be seen is that the change in phase constitution mainly occurred at the first 20 h, and then the transformed phases presented no change during the subsequent test. The main phase constitution change at the initial stage was that the original $Al_{0.47}Co_{0.53}$, AlCo, $Al_{80}Cr_{20}$, Co_3Ti, $CrSi_2$, CrB_2 phases were unstable in air atmosphere at elevated temperature, which reacted with oxygen and

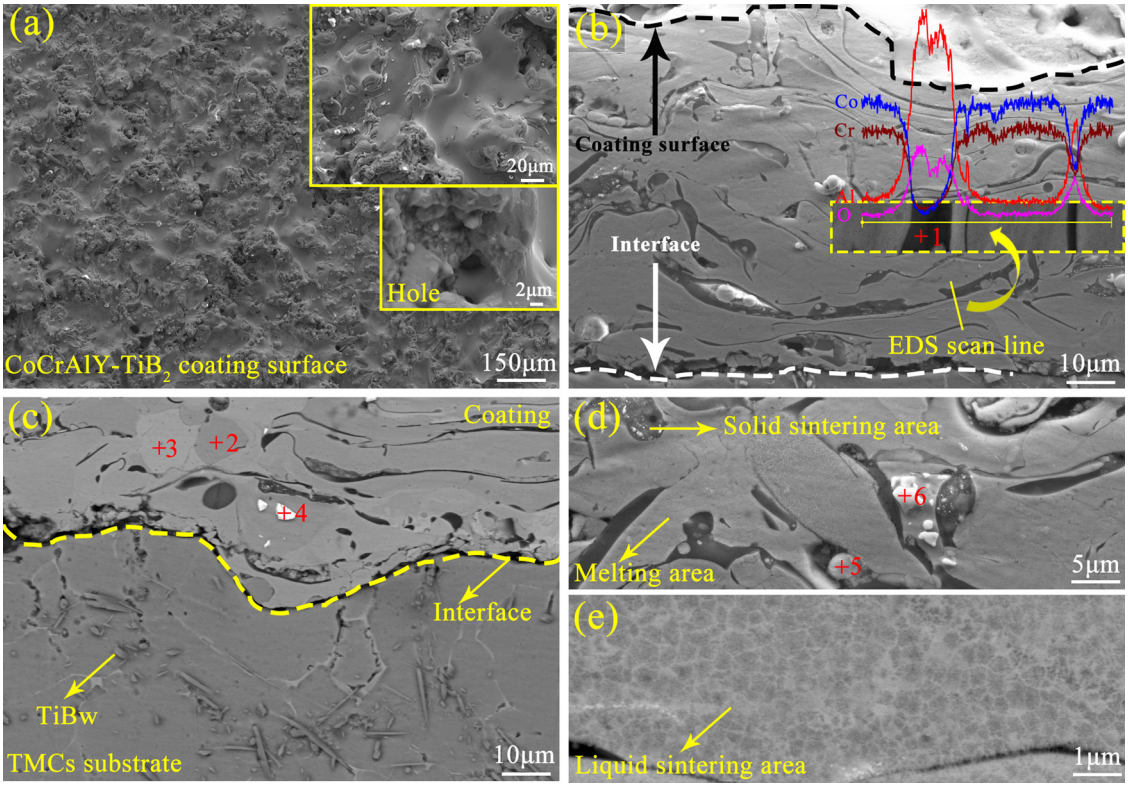

Fig. 7. The detailed microstructures of the coatings fabricated with the plasma power of 30.25 kW: (a) surface morphology; (b) the cross-sectional coating microstructures and EDS line scan profile; (c) the interfacial region between the coating and substrate; (d) higher magnification of the liquid sintering area; (e) higher magnification of the solid sintering and melting areas.

Table 4
EDS chemical composition of the coating regions marked "1-6″ in Fig. 7 (at. %).

Point	Co	Cr	Al	Ta	Y	Si	O	C	Possible phase
1	5.51	3.66	27.04	0.26	0.25	–	59.74	3.54	Al_2O_3
2	48.58	22.85	16.74	–	–	4.13	3.15	4.55	β-Al(Co, Cr)ss
3	53.79	27.10	9.75	3.48	–	–	2.73	3.16	γ-(Co, Cr)ss
4	10.81	7.22	2.02	29.81	–	11.15	4.27	34.72	TaC
5	52.06	23.64	6.38	10.17	–	2.36	1.50	3.89	γ-(Co, Cr)ss
6	4.49	3.41	–	40.25	0.49	–	5.75	45.61	TaC

then gradually transformed into Co, Al_2O_3, Cr_2O_3. Indicating that Co-CrAlY-TiB_2 coating exhibited an enhanced oxidation resistance by forming Al_2O_3 and Cr_2O_3 oxides. It is worth noting that the diffraction peak of residual AlCo and $Al_{0.47}Co_{0.53}$ solid solution phases ($2\theta = 44.7^{\circ}$) near the metallic Co peak was detected on the oxidized surface at 700 and 800 °C in Fig. 9(a) and (b), but disappeared after oxidizing at 900 °C (Fig. 9(c)). In reality, when oxidized at 700 °C, only a portion of Al element transformed into Al_2O_3, and the rest of Al remained as the original solid solution element state. Therefore, the diffraction peak of residual AlCo or $Al_{0.47}Co_{0.53}$ was detected in Fig. 9(a) and a certain amount of metallic Co also emerged during this stage. With the increase of oxidation temperature and duration, the quantity of residual AlCo or $Al_{0.47}Co_{0.53}$ phase on the oxidized surface gradually decreased and the corresponding diffraction peak intensity was reduced in Fig. 9(b) and even disappeared at 900 °C in Fig. 9(c) in association with the increased content of metallic Co. Moreover, there were also some differences in phase constitution change at various temperature. For instance, the diffraction peak of $AlCCr_2$ phase was observed when testing at 700 and 800 °C, which did not appear at 900 °C. Similarly, the $Al_{0.67}Cr_{0.08}Ti_{0.25}$ phase could only be detected at 800 °C. The possible reason accounting for this difference might be the instability of the corresponding phases in high-temperature environments.

The surface morphologies of the uncoated TiBw/Ti64 substrate after oxidation for 100 h are shown in Fig. 10. Fig. 10(a) indicates that oxide scales spalled during the test, and the surface morphologies were divided into four regions. Region "A" represented the exposed fresh surface formed when the oxide scale spalled, which presented a slight degree of oxidation. While region "B" revealed the morphology of the thick oxide scale, in which many cracks were initiated and propagated (Fig. 10). Based on the previous works [6,9,28], the oxide scale of TMCs were considered as needle-shaped TiO_2 and particle-shaped Al_2O_3. The thermal expansion coefficient difference between substrate and the oxide scale combined with the cyclic oxidation mode caused a certain thermal stress, which brought about the mechanical spallation [6]. Therefore, the oxide scale lost the protection capability, and the inferior oxidation resistance resulted in the rapid mass-gain rate illustrated in Fig. 8.

As for the coated samples by APS technology, all the oxidized surfaces illustrated in Fig. 11 were free of crack or mechanical spallation. Fig. 11(b) reveals that the oxide formed at 700 °C was fine and the as-sprayed coating microstructures were also observed, indicating a good oxidation resistance at this temperature. Combined with the EDS point analysis in Table 5, the granular Cr_2O_3 with a diameter of around 1 μm (region "1, 2″ in Fig. 11(b)) and fine Al_2O_3 were generated after oxidizing at 700 °C. Then the corresponding volume and quantity of oxide were enhanced when oxidized at 800 °C. During oxidation process, the stable TaC and SiC ceramic phases remained. While the γ-(Co, Cr)ss and β-Al(Co, Cr)ss reacted with oxygen and transformed into metallic Co, Al_2O_3, Cr_2O_3, $AlCCr_2$ etc. The oxide dimension was also enlarged over time. As a result, the comparatively continuous and dense Al_2O_3 and Cr_2O_3 oxide film formed at 800 °C (Fig. 11(d)) hindered the diffusion of oxygen into the substrate and prevented the substrate from internal oxidation. Moreover, not only the quantity and size, but also the compactness of the oxides formed at 900 °C were further increased as

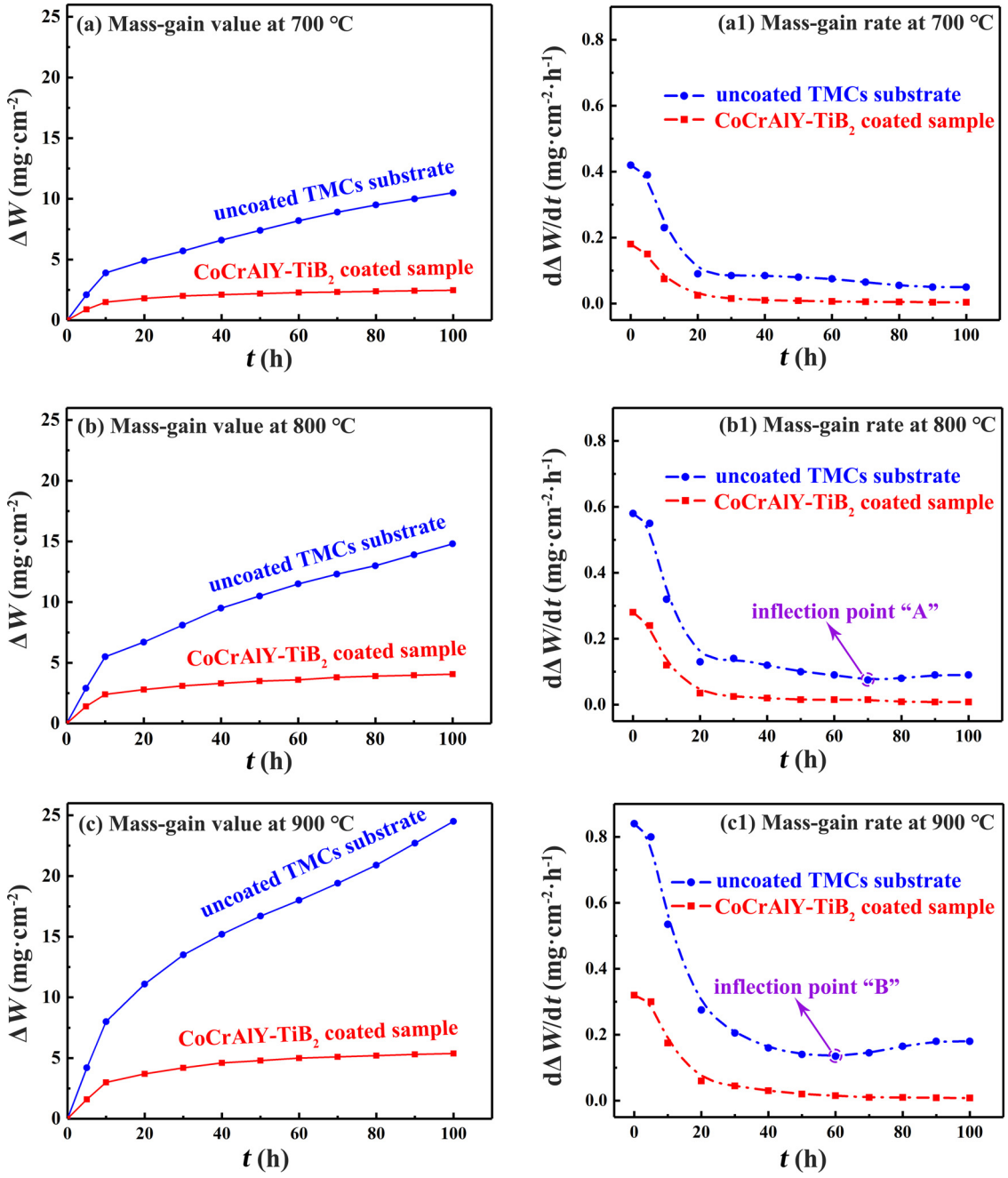

Fig. 8. The cycle oxidation kinetic curves of CoCrAlY-TiB_2 coated sample and uncoated TMCs substrate under different 700 °C, 800 °C and 900 °C: (a) (b) (c) mass-gain value; (a1) (b1) (c1) mass-gain rate.

shown in Fig. 11(e, f). Due to the poor electrical conductivity of Al_2O_3 and Cr_2O_3, some white patterns appeared on the secondary electron image (Fig. 11(e)) referring to the oxide with large scales. In light of Fig. 9, the transformed oxides were relatively stable since the oxide types did not change during oxidation process. Therefore, the uniform and dense oxides without any crack illustrated in Fig. 11(e, f) contributed to the excellent oxidation resistance of CoCrAlY-TiB_2 coating.

Fig. 12 reveals the EDS line profile at interface between the coating and substrate after oxidation for 100 h at 800 °C, indicating that Ti element diffused into the coating zone from the substrate which was beneficial for the interfacial bonding. As a result, the Ti diffusion layer with a thickness of around 5 μm and a closely jointed interface are presented in Fig. 12. Moreover, Co element also diffused into the substrate from the coating with a distance of about 1 μm. As for the O element, the corresponding content was rapidly reduced at the interface. Consequently, the oxygen diffusion behavior was hindered by the CoCrAlY-TiB_2 composite coating during oxidation at high-temperature environment.

3.4. Oxidation mechanisms

In light of the aforementioned experimental results, the poor anti-oxidation performance of the network structured TMCs has been significantly improved by the APS-deposited CoCrAlY-TiB_2 composite coating. In addition, the enhanced bonding strength suppressed the coating from mechanical spallation during oxidation and further improved the physicochemical stability. During the initial oxidation stage, the formation of oxide film led to the relatively rapid oxidation rate. With the extension of oxidation time, the thickness and density of the oxide film gradually increased, resulting in a better oxygen diffusion

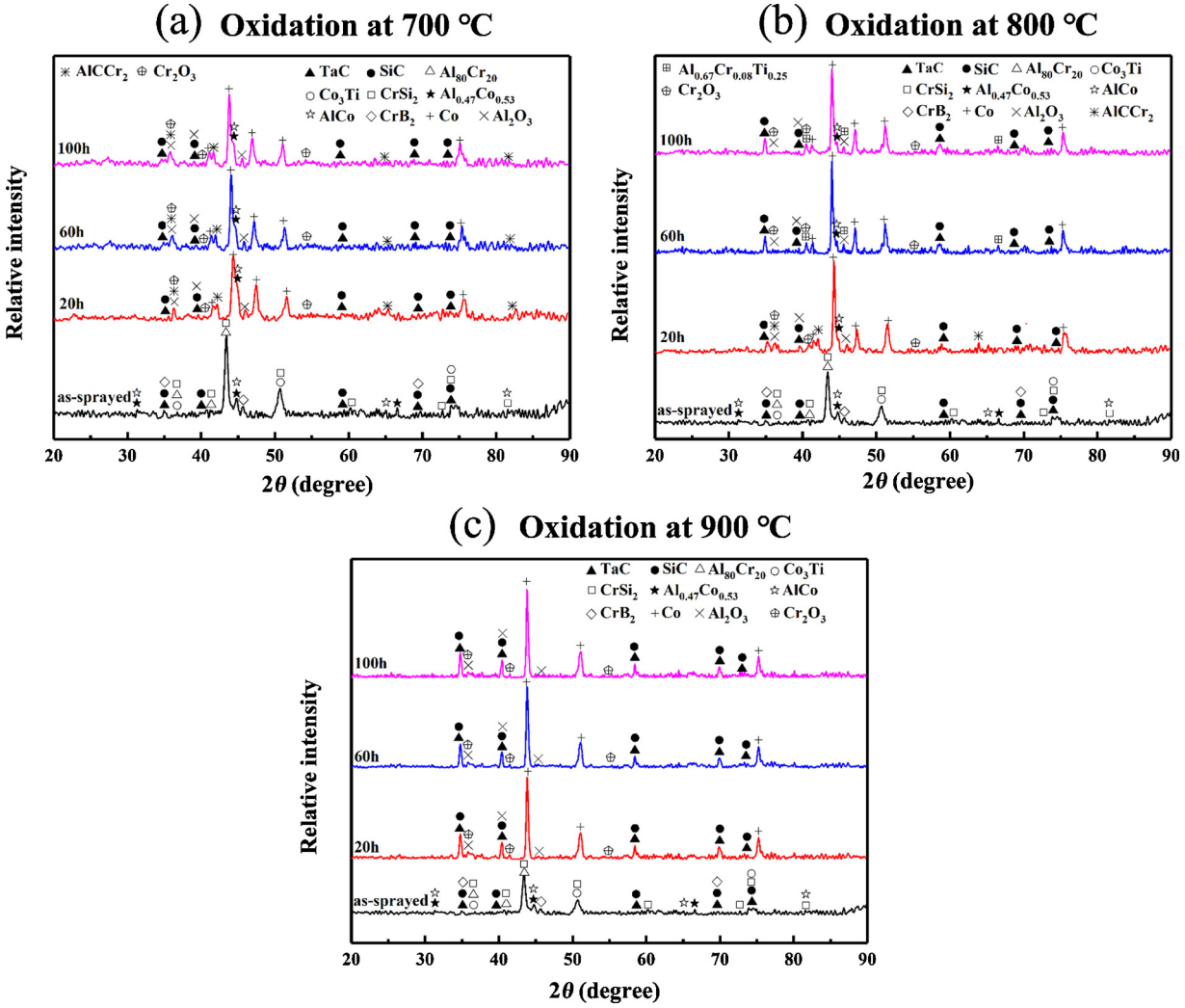

Fig. 9. XRD patterns of the CoCrAlY-TiB_2 composite coatings during oxidation test at (a) 700 °C, (b) 800 °C and (c) 900 °C.

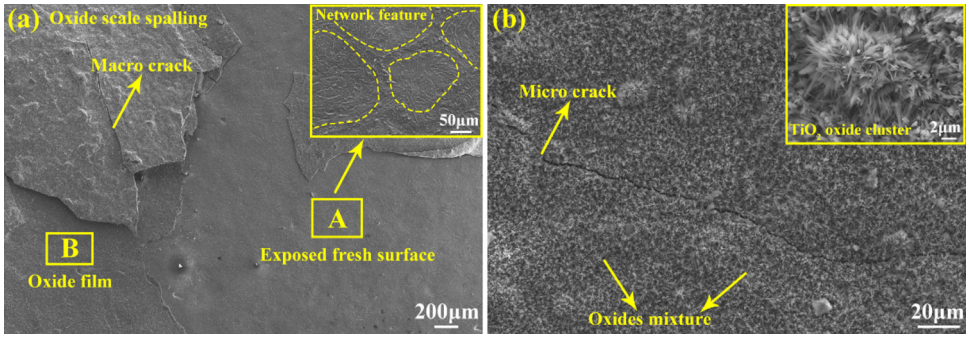

Fig. 10. Surface morphologies after oxidation test of the uncoated substrate at 800 °C: (a) an overview of the oxidized surface; (b) higher magnification of zone "B" in Fig. 10(a).

barrier effect. In reality, the oxidation resistance mainly depended on the stress state and properties of the oxide film. Based on the theory of Pilling-Bedworth ratio (PBR) for metals, the volume change due to the oxide formation could be expressed as Eq. (1) [29]:

$$PBR = \frac{V_{ox}}{V_m} = \frac{M_r \rho_m}{n A_r \rho_{ox}} \quad (1)$$

where M_r is the relative molecular weight of the metallic oxide, A_r represents the relative atomic mass of the metal, n is the metal ion valence in the oxide, ρ_m is the density of the metal ($kg{\cdot}m^{-3}$), ρ_{ox} represents the density of the oxide ($kg{\cdot}m^{-3}$). It was previously reported that when PBR > 1, a compressive stress would be developed in the oxide scale, while a tensile stress was generated in the scale with PBR < 1 [29]. As a result, the oxide scale would easily spall under the tensile stress or the excessive compressive stress. While the dense oxide film could be formed under a moderate compressive stress with a PBR value between 1 and 2.5 resulting in an excellent oxidation resistance. In this work, the oxide film was mainly composed of Al_2O_3 and Cr_2O_3 with a favorable PBR of 1.28 and 1.99, respectively. Therefore, the coating surface could be covered with a dense oxide scale, contributing to the remarkable

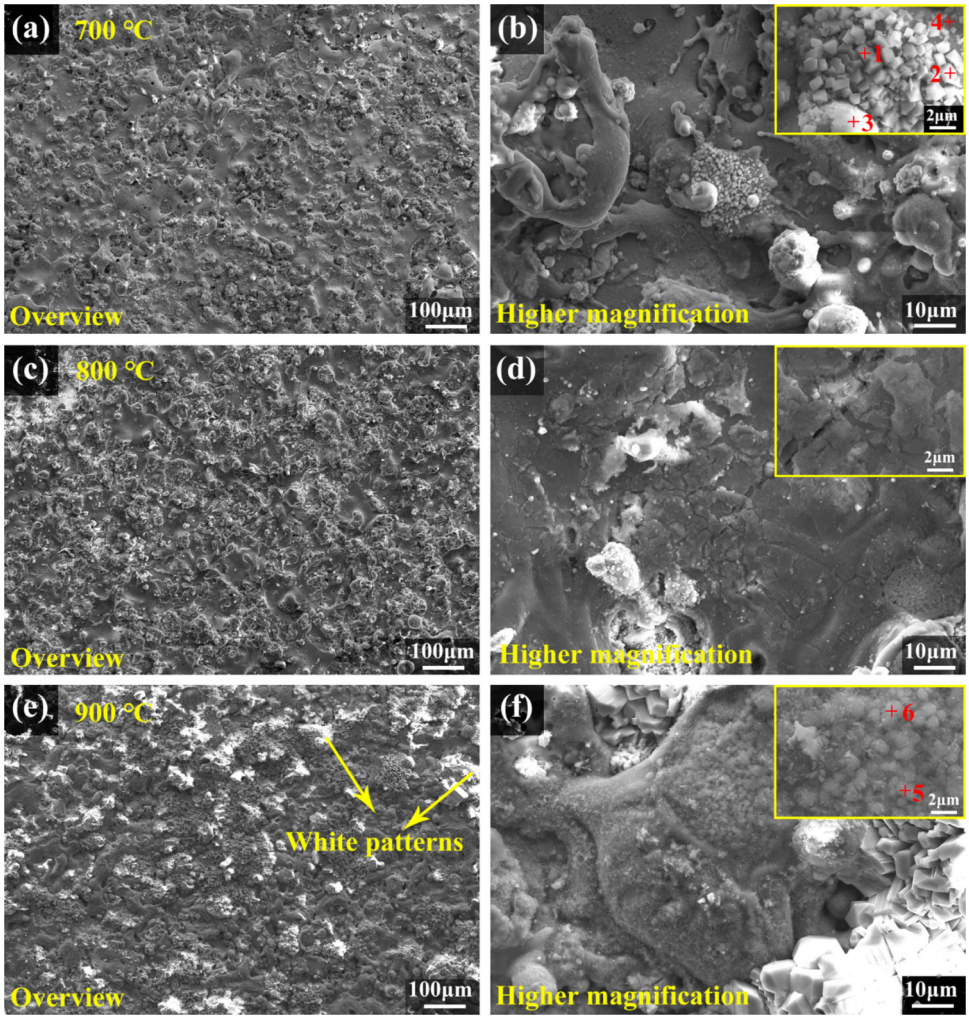

Fig. 11. Surface morphologies of the oxidized CoCrAlY-TiB_2 coating surfaces at (a, b) 700 °C, (c, d) 800 °C and (e, f) 900 °C.

Table 5
EDS chemical composition of the coating regions marked "1-6″ in Fig. 11 (at. %).

Point	Co	Cr	Al	Ta	Si	O	C	Possible phase
1	15.3	12.2	1.3	–	–	57.0	14.2	Co + Cr_2O_3
2	19.6	13.3	1.9	–	0.7	52.9	11.6	Co + Cr_2O_3
3	29.3	14.2	10.0	–	–	24.0	22.4	Co + Cr_2O_3 + Al_2O_3
4	21.5	10.5	5.4	1.2	–	48.7	12.7	Co + Cr_2O_3 + Al_2O_3
5	8.6	6.2	23.9	–	–	48.3	13.0	Cr_2O_3 + Al_2O_3
6	7.8	11.9	22.3	0.5	–	45.4	12.1	Cr_2O_3 + Al_2O_3

enhancement of anti-oxidation performance.

The oxidation reaction of alloy could be described as:

$$M_i + \frac{1}{2}O_2 = M_iO \tag{2}$$

During this reaction, the ions and electrons would diffuse at the metal/oxide interface, and the electrical conductivity of the oxide would affect the diffusion rate. Therefore, the poor conductivity of the dense Al_2O_3 (10^{-7} S·cm^{-1}) and Cr_2O_3 (10^{-1} S·cm^{-1}) scale formed on the CoCrAlY-TiB_2 coating surface reduced the oxidation rate. Moreover, the oxygen partial pressure in the gas atmosphere should also be greater than the pressure required for the metal–metal oxide equilibrium, which is provided by Eq. (3) [30]:

$$\left(P_{O_2}\right)^{1/2}{}_{M_i-M_iO} = \frac{\exp(\Delta G^0_{M_iO}/RT)}{\alpha_{M_i}} \tag{3}$$

Where, $(P_{O_2})_{M_i-M_iO}$ is the oxygen partial pressure of the metal-oxide equilibrium, $\Delta G^0_{M_iO}$ is the standard Gibbs free energy of M^iO formation (kJ·mol^{-1}), T is the absolute temperature, α_{M_i} is the activity of M_i in the alloy (mol·L^{-1}). Accordingly, Guo et al. hypothesized oxides of individual metallic element in the alloy were produced at the initial stage due to the sufficient oxygen pressure, while the most thermodynamically stable oxide would eventually cover the alloy surface as a result of selective oxidation [30]. Therefore, the most stable Al_2O_3 should be the only oxide. However, Cr_2O_3 was also detected in the oxidized CoCrAlY-TiB_2 composite coating, indicating that the oxide formation was controlled by the kinetic factor simultaneously. According to the Wagner's theory, the minimum quantity of metallic atoms N_i could be obtained by the followed equation [30]:

$$N_i = \left(\frac{\pi g N_O D_O V_m}{3 D_i V_{ox}}\right)^{\frac{1}{2}} \tag{4}$$

Where, g is a constant, N_OD_O is the oxygen permeability in the alloy, V_m is the molar volume of the alloy, D_i is the diffusion coefficient of i element, and V_{ox} is the molar volume of the oxide. Besides, the effective diffusion coefficient (D_{eff}) influenced by grain boundary was also decided by Hart as [30]:

$$D_{eff} = (1 - f)D_b + fD_{gb} \tag{5}$$

Where, D_b is the bulk diffusion coefficient, D_{gb} is the diffusion

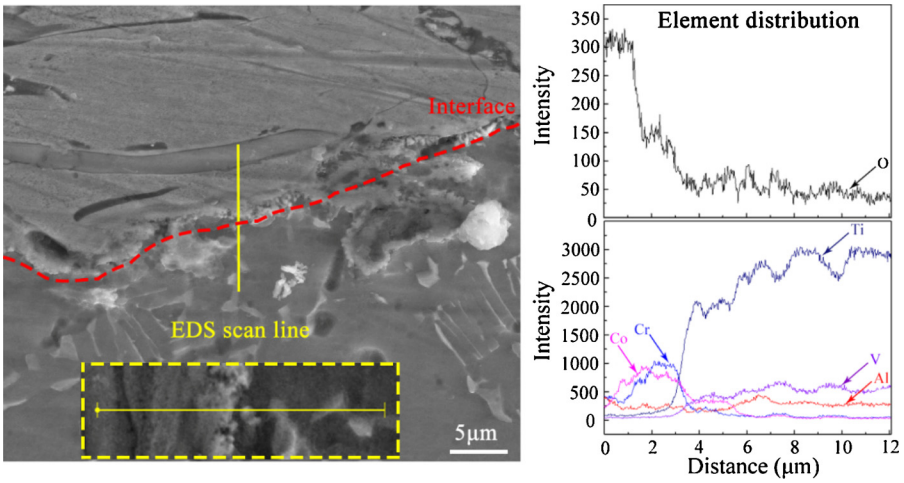

Fig. 12. The EDS element distribution at the interface after oxidation test at 800 °C.

coefficient along grain boundary, and f is the fraction of the atomic number in the grain boundary. As a result, Guo et al. reported that D_{eff} increased with the decrease of grain size. In this work, the CoCrAlY coating microstructures could be refined with the addition of 1 wt.% TiB_2 particles, which is attributed to two mechanisms based on our most recent report [31]. First, the deposit material experienced a rapid solidification process, during which the TiB_2 particles acted as energetically favored heterogeneous nucleation sites, enhancing the nucleation rate and refined the grains. Second, TiB_2 addition also enabled a strong pining effect on the grain boundary (Zener drag), which further hindered the grain growth kinetics. As a result, the microstructures of CoCrAlY-TiB_2 was refined compared with the traditional CoCrAlY coating. Therefore, refined microstructures led to an enhanced D_{eff}. Additionally, N_i was then decreased according to Eq. (4). Due to the comparatively low content of Ti (< 1 wt.%), TiO_2 could not be generated after oxidation. While the mass fraction of Cr and Al reached 57.36 wt.% and 12.74 wt.% respectively. Therefore, the corresponding oxide scale was finally composed of Cr_2O_3 and Al_2O_3 as supported by the XRD patterns in Fig. 9(b).

4. Conclusion

In summary, the CoCrAlY-TiB_2 composite coating was synthesized on the TMCs surface by APS technique to enhance the oxidation resistance. The microstructures were characterized and the cyclic oxidation behavior was elucidated in detail. The main findings are listed as follows:

(1) The optimized APS power was 30.25 kW, and the corresponding CoCrAlY-1TiB_2 (wt.%) coating was composed of TaC, SiC, Co_3Ti, $CrSi_2$, CrB_2, Al-rich β-(Co, Cr)Al and γ-(Co, Cr) solid solution phases;
(2) The bonding strength between the coating and substrate experienced an increase first and then decrease trend with the increase of APS power, and maximally reached 27.63 MPa. Besides, the TiB_2 addition was beneficial to improving the bonding strength when the power was higher than 27.50 kW, and the maximum enhancement was about 22.6% under 35.75 kW;
(3) The anti-oxidation performance was significantly enhanced by introducing CoCrAlY-TiB_2 composite coatings. Compared with the uncoated substrate, the weight gain of the coated specimens during cyclic oxidation test reduced by 66.7%, 73.1%, and 75.2% at 700, 800, and 900 °C, respectively. Such enhancement was attributed to the enhanced bonding strength and the formation of uniform and dense Al_2O_3 and Cr_2O_3 oxides which hindered internal oxidation.

Data availability

The raw/processed data required to reproduce these findings cannot be shared at this time due to technical or time limitations.

Acknowledgement

This work was financially supported by National Key R&D Program of China (No. 2017YFB0703100), National Natural Science Foundation of China (NSFC) under the Grant Nos. 51822103, 51731009 and 51671068, and Fundamental Research Funds for the Central Universities (No. HIT.BRETIV.201902).

References

[1] Y. Jiao, L. Huang, L. Geng, Progress on discontinuously reinforced titanium matrix composites, J. Alloys. Compd. 767 (2018) 1196–1215.
[2] L.J. Huang, L. Geng, H.X. Peng, Microstructurally inhomogeneous composites: Is a homogeneous reinforcement distribution optimal? Prog. Mater. Sci. 71 (2015) 93–168.
[3] S.C. Tjong, Y.W. Mai, Processing-structure-property aspects of particulate- and whisker-reinforced titanium matrix composites, Compos. Sci. Technol. 68 (2008) 583–601.
[4] L.J. Huang, L. Geng, H.X. Peng, K. Balasubramaniam, G.S. Wang, Effects of sintering parameters on the microstructure and tensile properties of in situ TiBw/Ti6Al4V composites with a novel network architecture, Mater. Des. 32 (2011) 3347–3353.
[5] Y. Jiao, L.J. Huang, L. Geng, X.T. Li, Y.N. Gao, M.F. Qian, R. Zhang, Nano-scaled Ti5Si3 evolution and Strength Enhancement of titanium matrix composites with two-scale architecture via heat treatment, Mater. Sci. Eng. A 701 (2017) 3559–3369.
[6] S.L. Wei, L.J. Huang, X.T. Li, Q. An, L. Geng, Interactive effects of cyclic oxidation and structural evolution for Ti-6Al-4V/(TiC+TiB) alloy composites at elevated temperatures, J. Alloys. Compd. 752 (2018) 164–178.
[7] C. Leyens, M. Peters, Titanium and Titanium Alloys: Fundamentals and Applications, John Wiley & Sons, Weinheim, 2003.
[8] D.A. Brice, P. Samimi, I. Ghamarian, Y. Liu, R.M. Brice, R.F. Reidy, J.D. Cotton, M.J. Kaufman, P.C. Collins, Oxidation behavior and microstructural decomposition of Ti-6Al-4V and Ti-6Al-4V-1B sheet, Corros. Sci. 112 (2016) 338–346.
[9] X.T. Li, L.J. Huang, S.L. Wei, Q. An, X.P. Cui, L. Geng, Cycle oxidation behavior and anti-oxidation mechanism of hot-dipped aluminum coating on TiBw/Ti6Al4V composites with network microstructure, Sci. Rep. 8 (2018) 5790.
[10] H. Asanuma, P. Polcik, S. Kolozsvari, F.F. Klimashin, H. Riedl, P.H. Mayrhofer, Cerium doping of Ti-Al-N coatings for excellent thermal stability and oxidation resistance, Surf. Coat. Tech. 326 (2017) 165–172.
[11] G. Shao, Q. Wang, X. Wu, C. Jiao, S. Cui, Y. Kong, J. Jiao, X. Shen, Evolution of microstructure and radiative property of metal silicide–glass hybrid coating for fibrous ZrO2 ceramic during high temperature oxidizing atmosphere, Corros. Sci. 126 (2017) 78–93.
[12] X. Gong, R.R. Chen, Y.H. Yang, Y. Wang, H.S. Ding, J.J. Guo, Y.Q. Su, H.Z. Fu, Effect of Mo on microstructure and oxidation of NiCoCrAlY coatings on high Nb containing TiAl alloys, Appl. Surf. Sci. 431 (2018) 81–92.
[13] Y. Han, Z. Zhu, B. Zhang, Y. Chu, Y. Zhang, J. Fan, Effects of process parameters of vacuum pre-oxidation on the microstructural evolution of CoCrAlY coating deposited by HVOF, J. Alloys. Compd. 735 (2018) 547–559.
[14] S. Salam, P.Y. Hou, Y.D. Zhang, H.F. Wang, C. Zhang, Z.G. Yang, Compositional

effects on the high-temperature oxidation lifetime of MCrAlY type coating alloys, Corros. Sci. 95 (2015) 143–151.
[15] N. Vermaak, A. Mottura, T.M. Pollock, Cyclic oxidation of high temperature coatings on new γ′-strengthened cobalt-based alloys, Corros. Sci. 75 (2013) 300–308.
[16] D. Zhang, J. Liu, Z. Xue, X. Mao, Oxidation behavior of T92 steel with NiCoCrAlY coating by EB-PVD, Surf. Coat. Tech. 252 (2014) 179–185.
[17] R. Chen, X. Gong, Y. Wang, G. Qin, N. Zhang, Y. Su, H. Ding, J. Guo, H. Fu, Microstructure and oxidation behaviour of plasma-sprayed NiCoCrAlY coatings with and without Ta on Ti44Al6Nb1Cr alloys, Corros. Sci. 136 (2018) 244–254.
[18] S. Deng, P. Wang, Y. He, J. Zhang, Surface microstructure and high temperature oxidation resistance of thermal sprayed NiCoCrAlY bond-coat modified by cathode plasma electrolysis, J. Mater. Sci. Technol. 33 (2017) 1055–1060.
[19] U. Schulz, O. Bernardi, A. Ebach-Stahl, R. Vassen, D. Sebold, Improvement of EB-PVD thermal barrier coatings by treatments of a vacuum plasma-sprayed bond coat, Surf. Coat. Tech. 203 (2008) 160–170.
[20] G. Hou, Y. An, X. Zhao, H. Zhou, J. Chen, Effect of alumina dispersion on oxidation behavior as well as friction and wear behavior of HVOF-sprayed CoCrAlYTaCSi coating at elevated temperature up to 1000 °C, Acta Mater. 95 (2015) 164–175.
[21] Z. Li, S. Qian, W. Wang, J. Liu, Microstructure and oxidation resistance of magnetron-sputtered nanocrystalline NiCoCrAlY coatings on nickel-based superalloy, J. Alloys. Compd. 505 (2010) 675–679.
[22] J.C. Pereira, J.C. Zambrano, M.J. Tobar, A. Yañez, V. Amigó, High temperature oxidation behavior of laser cladding MCrAlY coatings on austenitic stainless steel, Surf. Coat. Tech. 270 (2015) 243–248.
[23] L. Luo, H. Zhang, Y. Chen, C. Zhao, S. Alavi, F. Guo, X. Zhao, P. Xiao, Effects of the β phase size and shape on the oxidation behavior of NiCoCrAlY coating, Corros. Sci. 145 (2018) 262–270.
[24] J. Cai, Q. Guan, X. Hou, Z. Wang, J. Su, Z. Han, Isothermal oxidation behaviour of thermal barrier coatings with CoCrAlY bond coat irradiated by high-current pulsed electron beam, Appl. Surf. Sci. 317 (2014) 360–369.
[25] J. Cai, S.Z. Yang, L. Ji, Q.F. Guan, Z.P. Wang, Z.Y. Han, Surface microstructure and high temperature oxidation resistance of thermal sprayed CoCrAlY coating irradiated by high current pulsed electron beam, Surf. Coat. Tech. 251 (2014) 217–225.
[26] Y. Bai, Z.H. Han, H.Q. Li, C. Xu, Y.L. Xu, C.H. Ding, J.F. Yang, Structure–property differences between supersonic and conventional atmospheric plasma sprayed zirconia thermal barrier coatings, Surf. Coat. Tech. 205 (2011) 3833–3839.
[27] X. Zhang, M. Watanabe, S. Kuroda, Effects of processing conditions on the mechanical properties and deformation behaviors of plasma-sprayed thermal barrier coatings: evaluation of residual stresses and mechanical properties of thermal barrier coatings on the basis of in situ curvature measurement under a wide range of spray parameters, Acta Mater. 61 (2013) 1037–1047.
[28] Y. Jiao, L.J. Huang, S.L. Wei, L. Geng, M.F. Qian, S. Yue, Nano-Ti5Si3 leading to enhancement of oxidation resistance, Corros. Sci. 140 (2018) 223–230.
[29] C. Xu, W. Gao, Pilling-Bedworth ratio for oxidation of alloys, Mater. Res. Innovations 3 (2000) 231–235.
[30] M.H. Guo, Q.M. Wang, J. Gong, C. Sun, R.F. Huang, L.S. Wen, Oxidation and hot corrosion behavior of gradient NiCoCrAlYSiB coatings deposited by a combination of arc ion plating and magnetron sputtering techniques, Corros. Sci. 48 (2006) 2750–2764.
[31] S. Wei, L. Huang, X. Li, Y. Jiao, W. Ren, L. Geng, Network-strengthened Ti-6Al-4V/(TiC + TiB) composites: powder metallurgy processing and enhanced tensile properties at elevated temperatures, Metall. Mat. Trans A 50 (2019) 3629–3645.